

Stimulated generation: extraction of energy from balanced flow by near-inertial waves

Cesar B. Rocha^{1†}, Gregory L. Wagner² and William R. Young¹

¹Scripps Institution of Oceanography, University of California, San Diego

²Department of Earth, Atmospheric and Planetary Sciences, Massachusetts Institute of Technology

(Received xx; revised xx; accepted xx)

Key words:

1. Introduction

Geostrophic turbulence, a main paradigm of ocean mesoscale flows, transfers energy towards large scales. The energy flux out of the mesoscales en route to viscous dissipation, therefore, must involve ageostrophic dynamics. Indeed, existing studies advance a panoply of mechanisms to account for the required forward flow of energy. These include, but are not limited to, surface and benthic boundary turbulence and internal-wave generation by mesoscale eddies negotiating bottom topography (see Nagai *et al.* 2015, their figure 1, and references therein). But roughly half of the energy flux out of the mesoscales remains unaccounted for (Ferrari & Wunsch 2009; Nagai *et al.* 2015).

Recent research has suggested that the interaction of geostrophic flows with existing internal waves serves as a major sink of mesoscale energy (Xie & Vanneste 2015; Taylor & Straub 2016; Wagner & Young 2016; Barkan *et al.* 2016; Shakespeare & Hogg 2017). The emphasis on the energy extraction by *existing* internal waves—here denoted stimulated generation—contrasts with energy loss via spontaneous emission—a process by which internal waves are emitted during geostrophic adjustment. While spontaneous emission is localized at sharp fronts (large Rossby number, $Ro \gtrsim 1$) in the surface boundary layer (e.g., Shakespeare & Hogg 2017), stimulated generation operates at the small Rossby number ($Ro \ll 1$), quasi-geostrophic regime, both in the upper ocean and in the interior (e.g., Xie & Vanneste 2015).

To illuminate the physical mechanisms of energy extraction from barotropic flow by existing internal waves, we analyze a simple model of stimulated generation. This minimal model is a special family of solutions of the Xie & Vanneste (2015) equations, which couple the evolution of near-inertial waves (NIWs) with quasi-geostrophic (QG) flow. The focus on this specific class of wave-mean interactions is justified: geostrophic eddies are largely barotropic account for the bulk of the oceanic eddy kinetic energy (90%, Ferrari & Wunsch 2009), and near-inertial waves contain most of the oceanic high-frequency variability (Alford *et al.* 2016).

The main analytical result of this paper, an overlooked equation for the wave potential energy (3.5), clarifies the physics of quasi-inviscid stimulated generation associated with

† Email address for correspondence: crocha@ucsd.edu

vertical vorticity and lateral strain. The convergence of wave kinetic energy into anti-cyclones and the geostrophic straining of the wave field represent sources of wave potential energy—and sinks of geostrophic kinetic energy. Numerical solutions of initial-value problems confirm our interpretation of (3.5). And the solution diagnostics reveal that geostrophic straining is the main source of wave potential energy—and sink of geostrophic kinetic energy. In this quasi-inviscid limit, wave dispersion is the only mechanism that stops the energy conversion by moving the waves out of the straining regions.

2. The Xie & Vanneste (2015) minimal QG-NIW model

The Xie & Vanneste (2015) minimal model (Appendix A) assumes barotropic balanced flow, $\psi = \psi(x, y, t)$, uniform background buoyancy frequency, N_0 , f-plane, $\beta = 0$, and a single propagating wave mode in the vertical, e^{imz} , so that the total velocity (u, v, w) , pressure p , and buoyancy b are given by:

$$\text{\{L_velocity\}} \quad u + iv = e^{i(mz - f_0 t)} \phi - \psi_y + i\psi_x; \quad (2.1)$$

$$\text{\{L_velocity\}} \quad w = \frac{1}{2m} e^{i(mz - f_0 t)} (\phi_y - i\phi_x) + \text{cc}; \quad (2.2)$$

$$\text{\{pressure\}} \quad p = \frac{1}{2} f_0 \lambda^2 e^{i(mz - f_0 t)} (\phi_y - i\phi_x) + \text{cc} + f_0 \psi; \quad (2.3)$$

$$\text{\{buoyancy\}} \quad b = \frac{m}{2} f_0 \lambda^2 e^{i(mz - f_0 t)} (\phi_x + i\phi_y) + \text{cc}. \quad (2.4)$$

Above $\lambda = \frac{N_0}{f_0 m}$ is an intrinsic horizontal scale and cc denotes complex conjugate. And $\phi = \phi(x, y, t)$ is a complex near-inertial back-rotated velocity, which determines all wave fields in (2.1)–(2.4). In other words, with $\psi = 0$, (2.1)–(2.4) are wave polarization relations.

The balanced flow, whose streamfunction ψ determines all balanced fields in (2.1)–(2.4), satisfies the wave-averaged inversion relationship (cf. Wagner & Young 2015):

$$\text{\{qgpv\}} \quad q = \Delta\psi + \frac{1}{f_0} \left[\frac{1}{4} \Delta|\phi|^2 + \frac{i}{2} J(\phi^*, \phi) \right], \quad (2.5)$$

where $\Delta \stackrel{\text{def}}{=} \partial_x^2 + \partial_y^2$ is the horizontal Laplacian and $J(f, g) = f_x g_y - f_y g_x$ is the lateral Jacobian, and the superscript star $*$ denotes complex conjugation.

The balanced flow follows quasi-geostrophic potential-vorticity dynamics,

$$\text{\{macroturb\}} \quad q_t + J(\psi, q) = D_q, \quad (2.6)$$

and the wave velocity satisfies

$$\text{\{waves\}} \quad \phi_t + J(\psi, \phi) + \frac{i}{2} \phi \Delta \psi - \frac{i}{2} f_0 \lambda^2 \Delta \phi = D_\phi, \quad (2.7)$$

where is an intrinsic horizontal scale.

The wave equation (2.7) is similar to the Young & Ben Jelloul (1997) model. The back-rotated wave velocity evolves through dispersion—the last term in (2.7)—and advection and refraction by the geostrophic flow—the second and third terms in (2.7). But the wave equation (2.7) is non-linear owing to the quadratic wave terms in the quasi-geostrophic potential vorticity (2.5). In other words, the Young & Ben Jelloul (1997) near-inertial model is purely kinematic: the geostrophic flow evolves as if there were no waves and sets an inhomogeneous medium in which the waves propagate. But the Xie & Vanneste (2015) model is dynamic because both q and ϕ determine the flow: $\psi = \psi(x, y, t; q, \phi)$. Besides advection and refraction of waves by the geostrophic flow, these wave-mean interactions in (2.6)–(2.7) imply a positive finite-amplitude wave frequency shift (Appendix A).

The wave equation (2.7) resembles the reduced-gravity Young & Ben Jelloul model

derived by [Danioux *et al.* \(2015\)](#). Without advection, (2.7) is analogous to Schrodinger's equation (e.g., [Landau & Lifshitz 2013](#), pg. 51), with the relative vorticity, $\Delta\psi$, playing the role of the potential, and the dispersivity, $f_0\lambda^2$, as Planck's constant ([Danioux *et al.* 2015](#)).

The terms on the right of (2.6) and (2.7), D_q and D_ϕ , represent small-scale dissipation. The *ad hoc* introduction of these terms likely breaks the asymptotic ordering of the [Xie & Vanneste \(2015\)](#) model. But small-scale dissipation is necessary to absorb the forward transfers of potential enstrophy and wave kinetic and potential energies in the numerical simulations reported below. We find that biharmonic diffusion, e.g.,

$$D_q = -\kappa_e \Delta^2 q, \quad (2.8)$$

is sufficient to extend the spectral resolution compared to Laplacian diffusion, while avoiding obscure physical effects of higher-order diffusion or spectral filter. In practice, we choose the diffusivity that places the 35% highest modes in the dissipation range, so that aliased wavenumbers are strongly damped.

2.1. The WKB limit

An important feature of the wave equation (2.7) is that wave and balanced flow share the horizontal scales. In other words, the wave equation (2.7) isn't host to the WKB approximation (e.g., [Young & Ben Jelloul 1997](#)). But the WKB limit can be easily recovered. In this limit, plane-wave solutions, $\phi \sim e^{\mathbf{k}\cdot\mathbf{x} - \delta\omega t}$, yield the dispersion relationship

$$\frac{\delta\omega}{f_0} = \frac{1}{2}\lambda^2|\mathbf{k}|^2 + \frac{1}{f_0}\hat{\mathbf{z}} \cdot (\mathbf{k} \times \nabla\psi) + \frac{1}{2f_0}\Delta\psi, \quad (2.9) \quad \{\text{disp1}\}$$

where $\omega = f_0 + \delta\omega$ is the wave frequency, $\mathbf{k} = (k, l)$ is the horizontal wavevector, and $\hat{\mathbf{z}}$ is the vertical unit vector. The first term on the right of (2.9) is a linear approximation to the fractional change of the wave frequency about f_0 . The second term represents Doppler shift by large-scale geostrophic advection. And the last term is a frequency shift due to geostrophic vorticity ([Kunze 1985](#); [Young & Ben Jelloul 1997](#)).

2.2. Wave self-interaction and frequency shift

As remarked above, the the wave equation (2.7) is non-linear because both q and ϕ determine the flow ψ , which advects and refracts ϕ . The wave contribution to ψ is quadratic in ϕ (cf. (2.5)). Thus, the non-linear wave dynamics in (2.7) is cubic in ϕ . To study these non-linear wave effects, we linearize the QG-NIW equations about the exact solution $\phi = U_w = \text{real constant}$ and $\psi = 0$, so that $q = 0$. (Reality of Φ is assumed for algebraic simplicity below. But the final result is essentially unchanged with complex $\Phi = U_w + iV_w$ — U_w^2 is changed to $|\Phi|^2$.) The potential-vorticity equation (2.6) linearized about this state is trivial: $q_t = 0$, thus q remains zero. Also,

$$\Delta\psi = -\frac{U_w}{2f_0}\Delta\frac{1}{2}(\phi + \phi^*), \quad (2.10) \quad \{\text{lin_q}\}$$

where ϕ represents the small departure about U_w , so that the linearized wave equation becomes

$$\phi_t = \frac{i}{2} \left[\frac{U_w^2}{2f_0} \Delta\frac{1}{2}(\phi + \phi^*) + f_0\lambda^2\Delta\phi \right]. \quad (2.11)$$

Recalling that the wave velocity is $u_w + iv_w = e^{i(mz - f_0t)}\phi(x, y, t)$, the wave equation is recast:

$$\left[\partial_t^2 - \frac{1}{4}f_0\lambda^2 \left(f_0\lambda^2 + \frac{U_w^2}{2f_0} \right) \Delta^2 \right] v_w = 0, \quad (2.12)$$

where $\Delta^2 = (\partial_x^2 + \partial_y^2)^2$. Plane-wave solutions yield the dispersion relation

$$\frac{\delta\omega}{f_0} = \frac{1}{2}\lambda^2|\mathbf{k}|^2 \left[1 + \frac{1}{2}\frac{U_w^2}{f_0^2\lambda^2} \right]^{1/2}. \quad (2.13)$$

Thus, the wave self-interaction shifts the linear near-inertial frequency by

$$\left[1 + \frac{1}{2}\frac{U_w^2}{f_0^2\lambda^2} \right]^{1/2} - 1. \quad (2.14)$$

The frequency shift is positive definite and depends on the square of the ratio of the radius of the inertial circle U_w/f_0 to the intrinsic scale λ . If that ratio is small, then the frequency shift is $\approx U_w^2/(4f_0^2\lambda^2)$.

3. The physics of stimulated generation

3.1. Power integrals and energy conversion

From (2.7), we deduce that the near-inertial kinetic energy density $\frac{1}{2}|\phi|^2$ satisfies

$$\partial_t \frac{1}{2}|\phi|^2 + J(\psi, \frac{1}{2}|\phi|^2) + \underbrace{\nabla \cdot \left[\frac{1}{4}f_0\lambda^2 (\phi \nabla \phi^* - \phi^* \nabla \phi) \right]}_{\stackrel{\text{def}}{=} \mathbf{F}_w} = \frac{1}{2}(\phi^* D_\phi + \phi D_{\phi^*}). \quad (3.1)$$

Locally, $\frac{1}{2}|\phi|^2$ changes due to divergences of the geostrophic and wave fluxes and dissipation—the second, third, and fourth terms in (3.1). The wave flux \mathbf{F}_w is analogous to the probability current density of quantum mechanics (e.g., Landau & Lifshitz 2013, pg. 57). Using the polar representation $\phi = |\phi|e^{i\Theta}$ (e.g., Klein *et al.* 2004), we can unpack the wave flux:

$$\mathbf{F}_w = \frac{1}{4}f_0\lambda^2 (\phi \nabla \phi^* - \phi^* \nabla \phi) = f_0\lambda^2 \nabla \Theta \times \frac{1}{2}|\phi|^2, \quad (3.2)$$

where $f_0\lambda^2 \nabla \Theta = \frac{N_0^2}{f_0 m^2} \nabla \Theta$ is the generalized group velocity of hydrostatic near-inertial waves, which can be quickly verified under the plane-wave assumption, $\Theta = kx + ly$.

With simple boundary conditions, e.g., periodic or no normal flux, the wave kinetic energy budget is

$$\frac{d}{dt} \underbrace{\langle \frac{1}{2}|\phi|^2 \rangle}_{\stackrel{\text{def}}{=} K_w} = \varepsilon_\phi, \quad (3.3)$$

where angle brackets, $\langle \rangle$, represent average over the domain of area \mathcal{A} :

$$\langle f \rangle \stackrel{\text{def}}{=} \frac{1}{\mathcal{A}} \iint_{\mathcal{A}} f \, dx dy. \quad (3.4)$$

Also in (3.3), ε_ϕ is the rate of dissipation of wave kinetic energy (see appendix B for an explicit expression). In the inviscid limit, $\varepsilon_\phi \rightarrow 0$, the coupled model (2.6)-(2.7) conserves wave kinetic energy, K_w (Xie & Vanneste 2015).

Also from (2.7), we derive an equation for the wave potential energy $P_w \stackrel{\text{def}}{=} \frac{1}{2}\langle b^2 \rangle / N_0^2 = \frac{\lambda^2}{4} \langle |\nabla \phi|^2 \rangle$: $\frac{\lambda^2}{4} \langle \Delta \phi^* \times (2.7) + \Delta \phi \times (2.7)^* \rangle$ yields

$$\dot{P}_w = \underbrace{\frac{1}{f_0} \left\langle \frac{1}{2} \Delta \psi \nabla \cdot \mathbf{F}_w \right\rangle}_{\stackrel{\text{def}}{=} \Gamma_r} + \underbrace{\frac{\lambda^2}{2} \left\langle \frac{1}{2} \psi [J(\phi, \Delta \phi^*) + J(\phi^*, \Delta \phi)] \right\rangle}_{\stackrel{\text{def}}{=} \Gamma_a} + \chi_\phi, \quad (3.5)$$

where χ_ϕ is the dissipation of wave potential energy (see appendix B for explicit expressions).

And from (2.6), we form an equation for the geostrophic kinetic energy $K_e \stackrel{\text{def}}{=} \frac{1}{2} \langle |\nabla \psi|^2 \rangle$: $-\langle \psi \times (2.6) \rangle$, with (2.5), (3.1), (2.7), and multiple integration by parts, give

$$\dot{K}_e = -(\Gamma_r + \Gamma_a) + \Xi + \varepsilon_q, \quad (3.6) \quad \{\text{Ke}\}$$

where Ξ is a source of geostrophic kinetic energy due to wave dissipation and ε_q is the rate of dissipation of geostrophic kinetic energy (see appendix B for explicit expressions).

In the inviscid limit, $\chi_\phi \rightarrow 0$ and $\Xi \rightarrow 0$ and $\varepsilon_q \rightarrow 0$, the coupled model (2.6)-(2.7) conserves the energy (Xie & Vanneste 2015)

$$E \stackrel{\text{def}}{=} K_e + P_w. \quad (3.7) \quad \{\text{E}\}$$

In (3.6), $\Gamma_r + \Gamma_a$ is the conversion between geostrophic kinetic energy and wave potential energy. The term Γ_r stems from refraction and is easy to interpret: the convergence of the wave flux of kinetic energy density, $\nabla \cdot \mathbf{F}_w < 0$, into anticyclones, $\Delta \psi < 0$, is a source of wave potential energy, P_w . The term Γ_a stems from advection and resembles the source of variance of a passive scalar (tracer) gradient subject to lateral advection

$$c_t + J(\psi, c) = 0. \quad (3.8) \quad \{\text{c-t}\}$$

From (3.8), we deduce that $\langle \Delta c J(\psi, c) \rangle$ is the production of tracer-gradient variance, $\langle |\nabla c|^2 \rangle$. Analogously, Γ_a is the source of wave potential energy due to geostrophic straining. After multiple integration by parts, we rewrite this term as

$$\Gamma_a = \left\langle \begin{bmatrix} \phi_x^* & \phi_y^* \end{bmatrix} \mathbf{S} \begin{bmatrix} \phi_x \\ \phi_y \end{bmatrix} \right\rangle, \quad (3.9) \quad \{\text{gradphi}\}$$

where \mathbf{S} is the symmetric part of the geostrophic velocity gradient matrix,

$$\mathbf{S} \stackrel{\text{def}}{=} \begin{bmatrix} -\psi_{xy} & \frac{1}{2}(\psi_{xx} - \psi_{yy}) \\ \frac{1}{2}(\psi_{xx} - \psi_{yy}) & \psi_{xy} \end{bmatrix}, \quad (3.10)$$

whose sum of the elements squared (the Frobenius norm) is the variance of the geostrophic rate of strain. Hence, geostrophic straining enhances gradients of ϕ , thereby generating wave potential energy, P_w . When the geostrophic flow has a lateral scale much larger than the waves, this distortion of ϕ is akin to the wave capture mechanism of Bühler & McItyre (2005).

The standard Young & Ben Jelloul (1997) equation with barotropic geostrophic flow and single propagating vertical mode near-inertial also satisfies the potential energy equation (3.5). But Young & Ben Jelloul (1997) and subsequent studies overlooked the wave potential energy power integral, (3.5), or its generalization to baroclinic quasi-geostrophic flow. Of course, the standard Young & Ben Jelloul wave equation is uncoupled from the quasi-geostrophic potential vorticity equation, hence an increase in wave potential energy is not matched by a decrease in geostrophic kinetic energy.

3.2. Averaged equations and loss of coherence

The spatially-averaged (coherent) wave amplitude satisfies

$$\frac{d}{dt} \langle \phi \rangle + i \langle \frac{1}{2} \phi \Delta \psi \rangle = D_{\langle \phi \rangle}. \quad (3.11) \quad \{\text{phi_ave}\}$$

Introducing the decomposition $\phi = \langle \phi \rangle + \phi'$, we have

$$\frac{1}{2} \langle |\phi|^2 \rangle = \underbrace{\frac{1}{2} \langle \langle \phi \rangle^2 \rangle}_{\stackrel{\text{def}}{=} K_w^c} + \underbrace{\frac{1}{2} \langle |\phi'|^2 \rangle}_{\stackrel{\text{def}}{=} K_w^i}, \quad (3.12)$$

Thus, the kinetic energy of horizontally incoherent, ϕ' , and coherent, $\langle \phi \rangle$, waves satisfy

$$\{\text{Ki}w\} \quad \dot{K}_w^i = \Pi + \varepsilon_{\langle \phi \rangle}, \quad (3.13)$$

and

$$\{\text{Kc}w\} \quad \dot{K}_w^c = -\Pi + \varepsilon_{\phi'}, \quad (3.14)$$

with the kinetic energy transfer

$$\{\text{Pi}\} \quad \Pi = \frac{i}{2} [\langle \frac{1}{2} \phi \Delta \psi \rangle \langle \phi^* \rangle - \langle \frac{1}{2} \phi^* \Delta \psi \rangle \langle \phi \rangle], \quad (3.15)$$

which measures the loss of lateral coherence of the wave field. Also in (3.13) and (3.14), $\varepsilon_{\langle \phi \rangle}$ and $\varepsilon_{\phi'}$ are the dissipation of kinetic energy of incoherent and coherent waves, respectively.

3.3. Relevant parameters

Consider the scaling

$$\{\text{scaling}\} \quad \psi \sim U_e k_e^{-1}, \quad \text{and} \quad \phi \sim U_w, \quad (3.16)$$

with characteristic QG and NIW velocity scales U_e and U_w , and the characteristic horizontal length scale k_e^{-1} and time scale $(U_e k_e)^{-1}$. Using (3.16) in (2.6)-(2.7) reveals that there are two dynamically relevant parameters of the QG-NIW problem described by (2.6)-(2.7). First, the ‘wave amplitude’

$$\{\text{alpha}\} \quad \alpha \stackrel{\text{def}}{=} \underbrace{\frac{U_e k_e}{f_0}}_{\stackrel{\text{def}}{=} Ro} \times \left(\frac{U_w}{U_e} \right)^2, \quad (3.17)$$

measures the strength of the waves compared to the geostrophic flow and scales the contribution of the wave terms in the potential vorticity (2.5). Second, the ‘wave dispersivity,’

$$\{\text{hslash}\} \quad \hbar \stackrel{\text{def}}{=} f_0 \lambda^2 \times \frac{k_e}{U_e}, \quad (3.18)$$

scales the importance of linear dispersion, which extenuates the unsmoothing effects of advection and refraction.

3.4. Summary

The following initial value problem that idealizes the oceanographic post-storm scenario illuminates the physics of stimulated generation. Stormy winds impart momentum into the ocean, thereby generating near-inertial oscillations with a lateral decorrelation scale larger than the mesoscale eddies. The coupled model (2.6)–(2.7) describes the post-storm evolution of this initially coherent inertial oscillation (Xie & Vanneste 2015; Wagner & Young 2016). Geostrophic refraction concentrates the waves in anticyclones. The eddy-scale gradients of ϕ then support geostrophic advection. Advection and refraction reduce the lateral coherence of the waves—and wave dispersion counteracts this unsmoothing effect.

The explicit expression for energy conversion on the right of (3.5) clarifies the mechanisms of wave-mean energy exchange. First, refraction causes a convergence of wave

kinetic energy density in anticyclones. Then, advection strains the wave field, enhancing the gradients of wave velocity created by refraction. Both processes generate wave potential energy at the expenses of geostrophic kinetic energy, thus motivating the nomenclature ‘refraction sink’ ($-\Gamma_r$) and ‘advection sink’ ($-\Gamma_a$) of geostrophic kinetic energy.

The remaining of this paper verifies this thought experiment and quantifies the energy conversion by solving numerically two problems in which an initially perfectly coherent near-inertial oscillation interacts with the Lamb-Chaplygin dipole (Section 3) and with a turbulent field emergent from random initial conditions (Section 4).

4. An idealized solution: the Lamb-Chaplygin dipole

As a preamble to our discussion of the QG-NIW energy transfers in freely-evolving turbulence, we consider a simpler example in which the initial quasi-geostrophic flow is given the the Lamb-Chaplygin dipole. This dipole is an exact solution of the Euler equations on an infinite two-dimensional plane where the vorticity is confined to a circle of radius R (Meleshko & Van Heijst 1994). The solution, steady on a frame moving at uniform zonal velocity U_e , is

$$\Delta\psi = \frac{2U_e\kappa}{J_0(\kappa R)} \begin{cases} J_1(\kappa r)\sin\theta, & \text{if } r \leq R, \\ 0, & \text{if } r \geq R, \end{cases} \quad (4.1) \quad \{\text{lambda_q}\}$$

where $r^2 = (x - x_c)^2 + (y - y_c)^2$ is the radial distance about the dipole’s center (x_c, y_c) , $\tan\theta = (y - y_c)/(x - x_c)$, and J_n is the n ’th order Bessel function of first kind. The matching condition at $r = R$, $J_1(\kappa R) = 0$, determines κ ; the dipole is the first eigensolution, with eigenvalue $\kappa R \approx 3.8287$. If the wave potential vorticity is zero, then the dipole (4.1) is a solution of (2.6). This is the case when a uniform ϕ is used as initial condition (Sections 3 and 4).

The initial wave velocity is given by a uniform (i.e., perfectly coherent) near-inertial oscillation with speed U_w :

$$\phi(x, y, t = 0) = \frac{1+i}{\sqrt{2}} U_w. \quad (4.2) \quad \{\text{NIO}\}$$

4.1. Parameters inspired by the Ocean Storms Experiment

Inspired by the Ocean Storms Experiments (D’Asaro *et al.* 1995), we choose $U_e = 5 \times 10^{-2} \text{ m s}^{-1}$, $R = 2\pi/k_e = 84 \text{ km}$, and $f_0 = 10^{-4} \text{ s}^{-1}$ ($\sim 45^\circ\text{N}$), which gives $\text{Ro} \approx 3.75 \times 10^{-2}$. Strong storm over weak mesoscale flow generates strong near-inertial currents (D’Asaro *et al.* 1995). Choosing $U_w = 10 \times U_e = 10^{-1} \text{ m s}^{-1}$ yields a wave amplitude $\alpha \approx 3.75$. A NIW with a typical vertical wavelength, $2\pi/m = 325 \text{ m}$, and $N_0 = 50 \times f_0 = 5 \times 10^{-3} \text{ s}^{-1}$, yields a moderate dispersivity $\hbar \approx 1$.

4.2. Solution for $\hbar \approx 1$ and $\alpha \approx 3.75$

We solve the coupled model (2.6)-(2.7) subject to the initial conditions (4.1) and (4.2) and the parameters inspired by the Ocean Storms Experiment. We integrate the solutions numerically for 30 eddy-turnover time units, $30 \times (U_e k_e)^{-1} \approx 90 \text{ days}$, on a doubly periodic domain using standard Fourier pseudo-spectral methods (detail in appendix B). Dipole images, artifacts of periodization, cause a small zonal drift of the dipole. To render this drift negligible, we choose a domain size much larger than the dipole’s radius, $R/L \approx 0.06$. Table B.1 provides a full description of solution parameters.

Because the initial wave velocity is laterally uniform, refraction dominates the initial

evolution of the solution. Indeed, the solution presents a dramatic wave concentration in the anticyclone and wave expulsion from the cyclone in the first couple of eddy turnover time units, $(U_e k_e)^{-1}$. After $5 \times (U_e k_e)^{-1}$, there is a threefold modulation of the wave kinetic energy density on eddy scales (Figure 4.2). The correlation coefficient

$$\{corr_r\} \quad r \stackrel{\text{def}}{=} \frac{\langle |\phi'|^2 \Delta \psi \rangle}{\langle |\phi'|^4 \rangle^{1/2} \langle (\Delta \psi)^2 \rangle^{1/2}}, \quad (4.3)$$

quantifies the wave concentration in regions positive or negative vorticity; negative correlation, $r < 0$, indicates wave concentration in anticyclones (Danioux *et al.* 2015). Starting from the uniform wave initial condition, vorticity and incoherent wave kinetic energy density quickly become negatively correlated ($r = -0.75$ at $t \times U_e k_e = 2$; Figure 4.2d). This initial wave focusing in anticyclones is associated with a rapid increase in incoherent wave kinetic energy (Figure 4.2c) and a rapid increase of wave potential energy (Figure 4.2b). The gain of wave potential energy, initially dominated by the conversion due to refraction, Γ_r , occurs at the expenses of geostrophic kinetic energy (Figure 4.2a): the dipole's kinetic energy decays by about 20% in two eddy-turnover time units. The strong wave concentration in the negative vorticity region, and the accompanying geostrophic energy loss, weakens the anticyclone. This asymmetry in wave concentration tilts the dipole and the vortex self-induced zonal velocity no longer matches the downstream uniform flow: the dipole starts to drift upstream at $t \times U_e k_e \approx 5$.

The eddy-scale gradients in wave velocity, which are created by refraction, allow for the other mechanisms in the wave equation (2.7) to become important. Linear dispersion radiates waves from the dipole, with horizontal scales comparable to k_e^{-1} . And geostrophic advection starts to enhance the refraction-created gradients. As a consequence of these two processes becoming important, the correlation r decreases.

The advective conversion, Γ_a , kicks off at $t \times U_e k_e \approx 4$ (Figure 4.2b), and takes over the Γ in few eddy-turnover time units. Contemporarily, the wave-induced quasi-geostrophic flow strains the anticyclone, which develops a filamentary structure. Because most of the advective energy conversion occurs in the anticyclone, the negative correlation r decreases further, and becomes positive at $t \times U_e k_e \approx 7$. At this point, Γ_r becomes weakly negative (i.e., from waves to geostrophic flow), though the total conversion, $\Gamma_r + \Gamma_a$, remains positive thanks to a strong positive advective conversion. The energy conversion nearly halts at $t \times U_e k_e \approx 20$.

Because the advective conversion, Γ_a , remains positive for the duration of the simulation, Γ_a accounts for the bulk conversion of energy from geostrophic flow to waves. Indeed, the time-integrated Γ_a accounts for 77.5% of total geostrophic kinetic energy change (Table 1); the time-integrated refraction conversion, Γ_r , represents 22.7% of the geostrophic kinetic energy changes. And direct dissipation and wave-dissipation source (Appendix B) account for the residual changes ($< 1\%$).

5. Macroturbulence solutions: decaying barotropic flow

To study the energy exchange between near-inertial waves and quasi-geostrophic flow in a turbulent regime relevant to the ocean, we consider a barotropic flow that emerges from random initial conditions integrated for 20 eddy turnover time units. In other words, we first integrate the initial condition

$$\{\psi_{init}\} \quad \psi(x, y, t \times U_e k_e = -20) = \sum_{k,l} |\hat{\psi}| \cos(kx + ly + \chi_{k,l}) \quad (5.1)$$

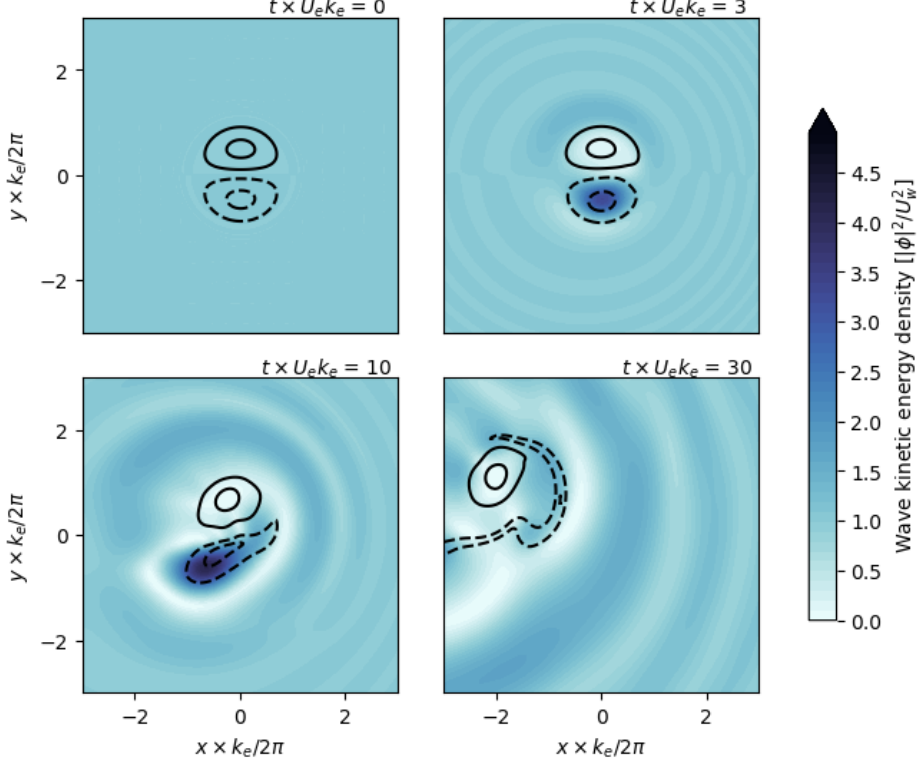


FIGURE 1. Snapshots of the Lamb-Chaplygin dipole solution with $\hbar \approx 1$ and $\alpha \approx 3.75$. Colors represent wave kinetic energy density, $|\phi'|^2/U_w^2$. Contours represent potential vorticity, $q/(U_e k_e) = [-1.5, -0.5, 1.5, 0.5]$, with dashed lines showing negative values. These plots only show the central $(1/5)^2$ of the simulation domain. (The supplemental material contains a video of the simulation.)

TABLE 1. The time-integrated budget of wave potential energy and quasigeostrophic kinetic energy of the Lamb-Chaplygin dipole experiment.

\dot{P}_w budget	Rel. contribution ($\int \dot{P}_w dt / \Delta P_w$)	\dot{K}_e budget	Rel. contribution ($\int \dot{K}_e dt / \Delta K_e$)
Γ_r	0.228	$-\Gamma_r$	-0.227
Γ_a	0.778	$-\Gamma_a$	-0.774
—	—	Ξ_r	0.004
—	—	Ξ_a	0.0
χ_ϕ	-0.006	ϵ_ψ	-0.003
Res.	0.0	Res.	0.0

with waveless QG dynamics before introducing waves at $t \times U_e k_e = 0$. In 5.1, $\chi_{k,l}$ is a random phase uniformly distributed on $[0, 2\pi)$, and $|\hat{\psi}|$ is the streamfunction isotropic spectrum

$$|\hat{\psi}| = C \times \{ |k| [1 + (|k|/k_e)^4] \}^{-1/2}, \quad (5.2) \quad \{\text{psih_mag}\}$$

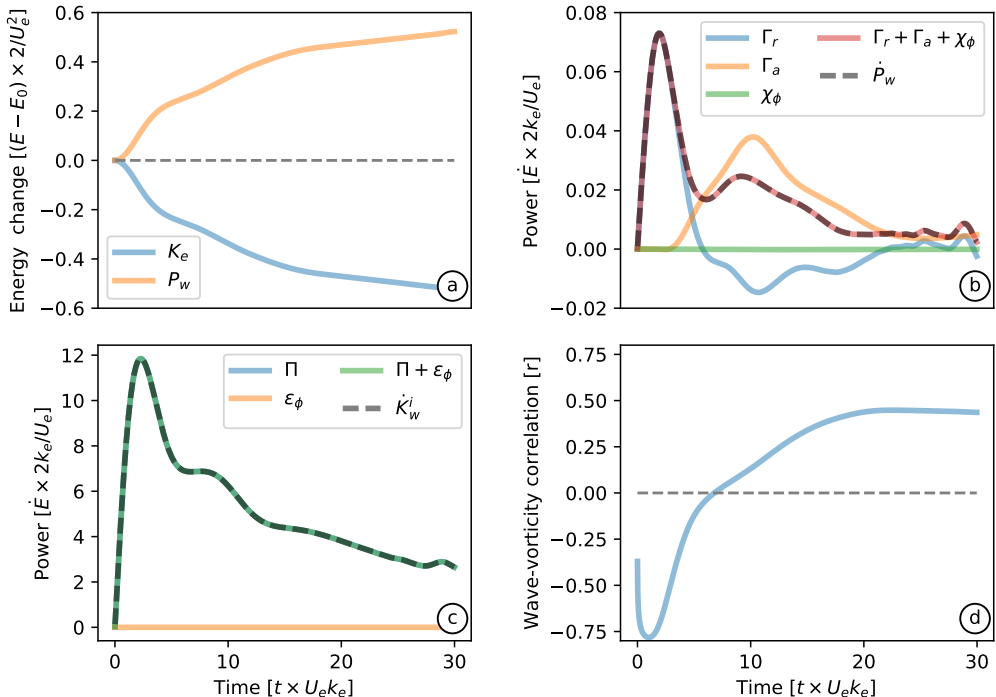


FIGURE 2. Statistics of the Lamb-Chaplygin dipole solution with $\hbar \approx 1$ and $\alpha \approx 3.75$. (a) Energy change about initial condition. (b) Wave potential energy budget (3.5). (c) Incoherent wave kinetic energy budget (3.13). (d) Coefficient of correlation between incoherent wave kinetic energy and geostrophic relative vorticity (4.3).

with the wavenumber magnitude $|k|^2 = k^2 + l^2$. The prescribed initial energy $U_e^2/2$ determines the constant C:

$$\sum_{k,l} \underbrace{|k|^2 |\hat{\psi}|^2}_{\stackrel{\text{def}}{=} \mathcal{K}_e} = \frac{1}{2} U_e^2. \quad (5.3) \quad \{\text{ke_init}\}$$

The kinetic energy spectrum, \mathcal{K}_e , peaks at the energy-containing scale k_e^{-1} . At scales larger than k_e^{-1} , \mathcal{K}_e has a linear dependence on $|k|$, whereas \mathcal{K}_e decays as $|k|^{-3}$ at scales smaller than k_e^{-1} . This red spectrum ensures insignificant energy dissipation by the biharmonic diffusivity in (2.6).

The evolution of a random initial condition constrained by the quasi-inviscid quasi-geostrophic dynamics (2.6) has been well studied, beginning with [Fornberg \(1977\)](#). Stirring of vorticity, $\Delta\psi$, by the flow, ψ , transfers enstrophy towards small scales; energy flows to large scales. Most of enstrophy is dissipated within few eddy turnover time units, whereas kinetic energy is nearly conserved. Vorticity concentrates into localized structures: after 20 eddy turnover time units, the vorticity is well-organized into a sea of coherent vortices that form via like-sign vortex merging (e.g., [McWilliams 1984](#)).

We add a perfectly coherent near-inertial oscillation (4.2) to the mature barotropic turbulence at $t \times U_e k_e = 0$. For all parameters considered in the remaining of this paper, there are no qualitative long-term differences between the solutions described below and results from introducing the waves at $t \times U_e k_e = -20$.

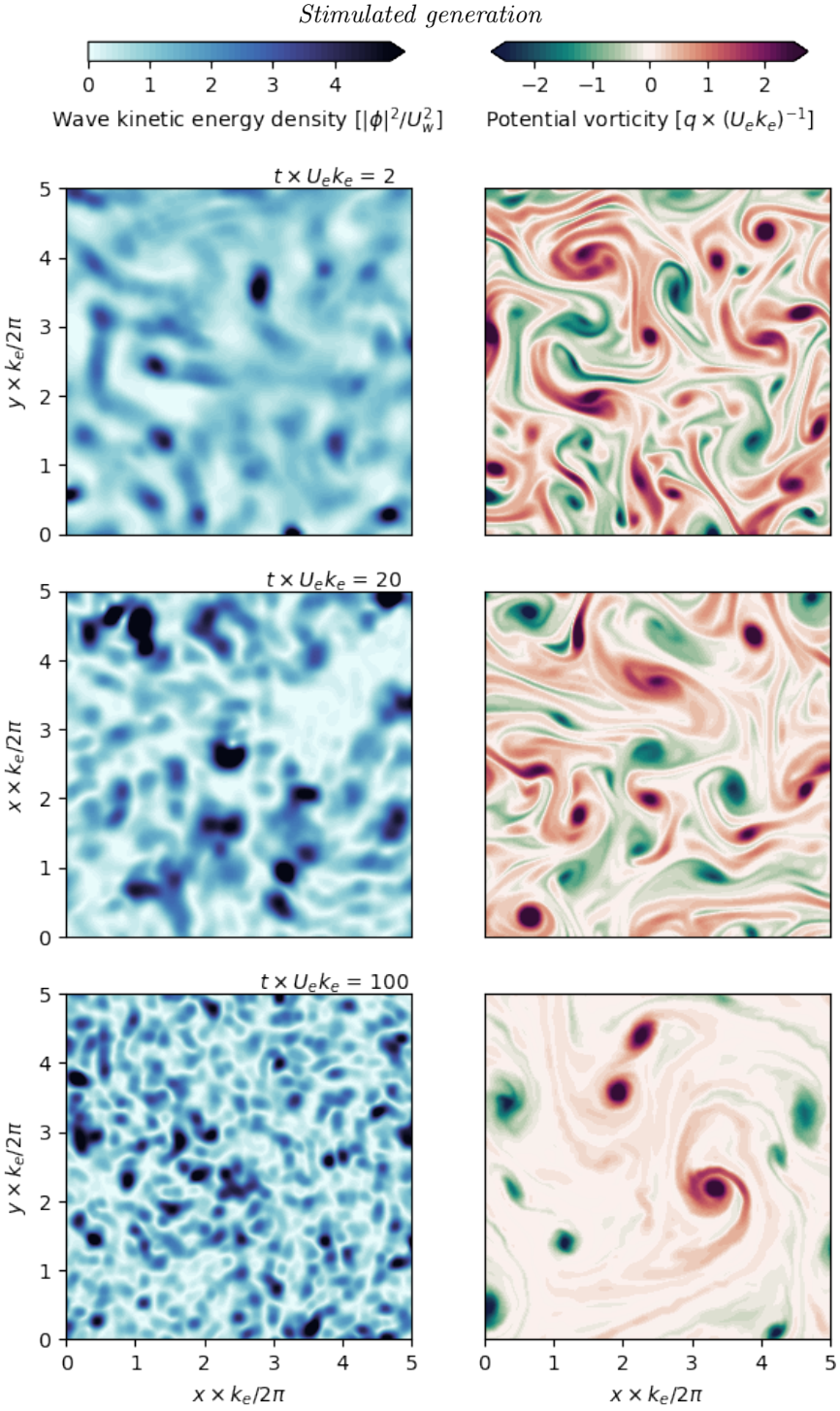


FIGURE 3. Snapshots of the decaying turbulence solution with $\hbar \approx 1$ and $\alpha \approx 1$. Left panels: wave kinetic energy density. Right panels: potential vorticity. These plots only show the bottom-left $(1/2)^2$ of the simulation domain. (The supplemental material contains a video of the simulation.)

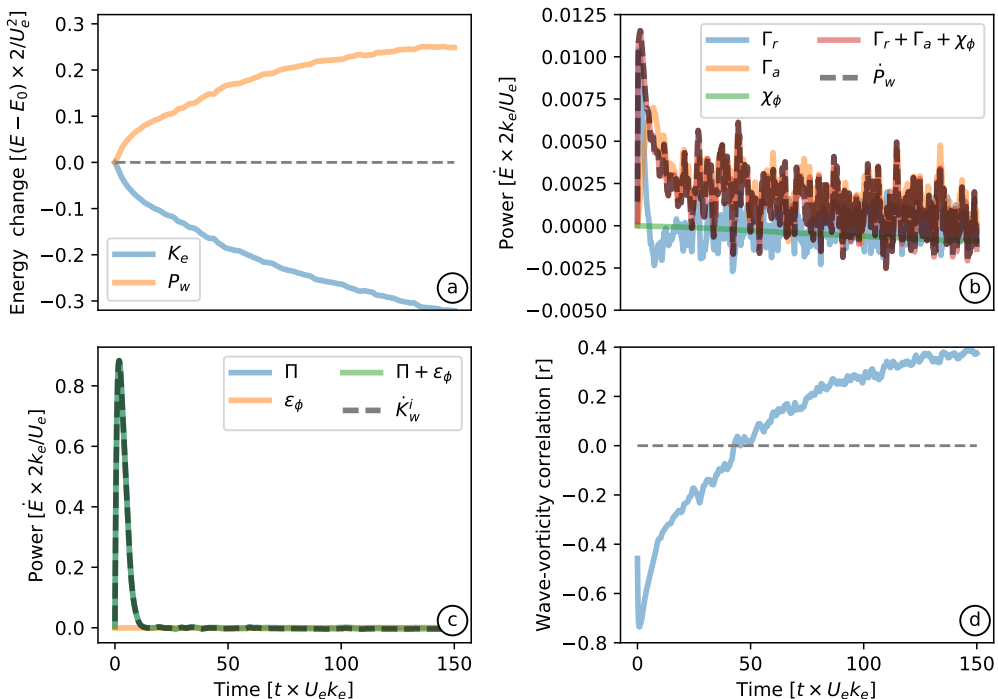


FIGURE 4. Statistics of the decaying turbulence solution with $\hbar \approx 1$ and $\alpha \approx 1$. (a) Energy change about initial condition. (b) Wave potential energy budget (3.5). (c) Incoherent wave kinetic energy budget (3.13). (d) Coefficient of correlation between incoherent wave kinetic energy and relative vorticity (4.3).

TABLE 2. The time-integrated budget of wave potential energy and quasigeostrophic kinetic energy of the decaying turbulence dipole experiment.

\dot{P}_w budget	Rel. contribution ($\int \dot{P}_w dt / \Delta P_w$)	\dot{K}_e budget	Rel. contribution ($\int \dot{K}_e dt / \Delta K_e$)
Γ_r	-0.002	$-\Gamma_r$	0.002
Γ_a	1.274	$-\Gamma_a$	-0.986
—	—	Ξ_r	0.058
—	—	Ξ_a	-0.003
χ_ϕ	-0.272	ϵ_ψ	-0.071
Res.	0.0	Res.	0.0

5.1. Parameters for strong mid-latitude macroturbulence

Consider strong mid-latitude macroturbulence, such as the Gulf Stream or Kuroshio Extension. The choice of parameters, $U_e = 0.1 \text{ m s}^{-1}$, $f_0 = 1 \times 10^{-4} \text{ s}^{-1}$, $2\pi k_e^{-1} = 125 \text{ km}$ gives a Rossby number $Ro \approx 0.05$. For reference, the eddy-turnover scale is $(U_e k_e)^{-1} \approx 5.8$ days. Strong near-inertial velocity imparted by atmospheric storms, $U_w \sim \sqrt{2}U_e$, implies a wave amplitude

$$\alpha \approx 0.1. \quad (5.4)$$

A near-inertial vertical wavelength of $\lambda_z = 2\pi/m = 300 \text{ m}$ (e.g., Alford *et al.* 2016) on a strongly stratified upper ocean, $N_0/f_0 = 100$, yields a dispersivity

$$\hbar \approx 1.0. \quad (5.5)$$

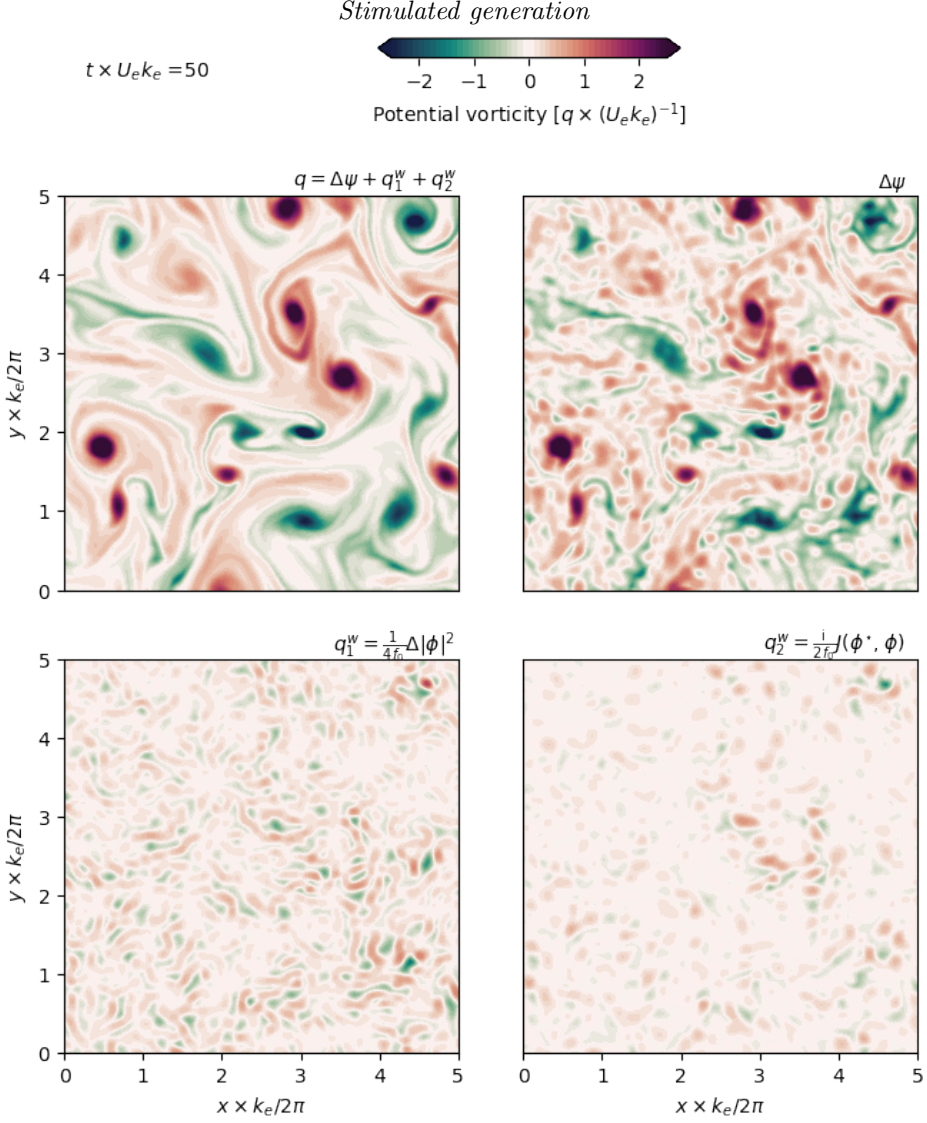


FIGURE 5. Snapshot of quasi-geostrophic potential vorticity of the decaying turbulence solution with $\hbar \approx 1$ and $\alpha \approx 1$, at $t \times U_e k_e = 50$. The potential vorticity, q , is decomposed into relative vorticity, $\Delta\psi$, and the two terms of the wave potential vorticity, q_1^w and q_2^w .

5.2. Solutions for $\hbar = 1$ and $\alpha = 0.1$

The decaying turbulence experiment with $\hbar = 1$ and $\alpha = 0.1$ qualitatively resembles the Lamb-Chaplygin solution. Starting from a uniform wave field, refraction quickly concentrates the waves into anticyclones. By $t \times U_e k_e \approx 2$ there is a four-fold modulation of the wave kinetic energy density on eddy scales (Figure 5), reducing the lateral coherence of the waves (Figure 5c). This initial wave concentration into anticyclones is dramatic, $r < -0.75$, thereby causing a rapid wave potential energy gain at the expenses of geostrophic kinetic energy loss (Figure 5a).

The eddy-scale gradients of wave velocity support geostrophic advection and wave dispersion. Indeed, the advective conversion, Γ_a , quicks off once refraction imprints eddy scales on the wave field. Both advection and wave dispersion reduce the wave

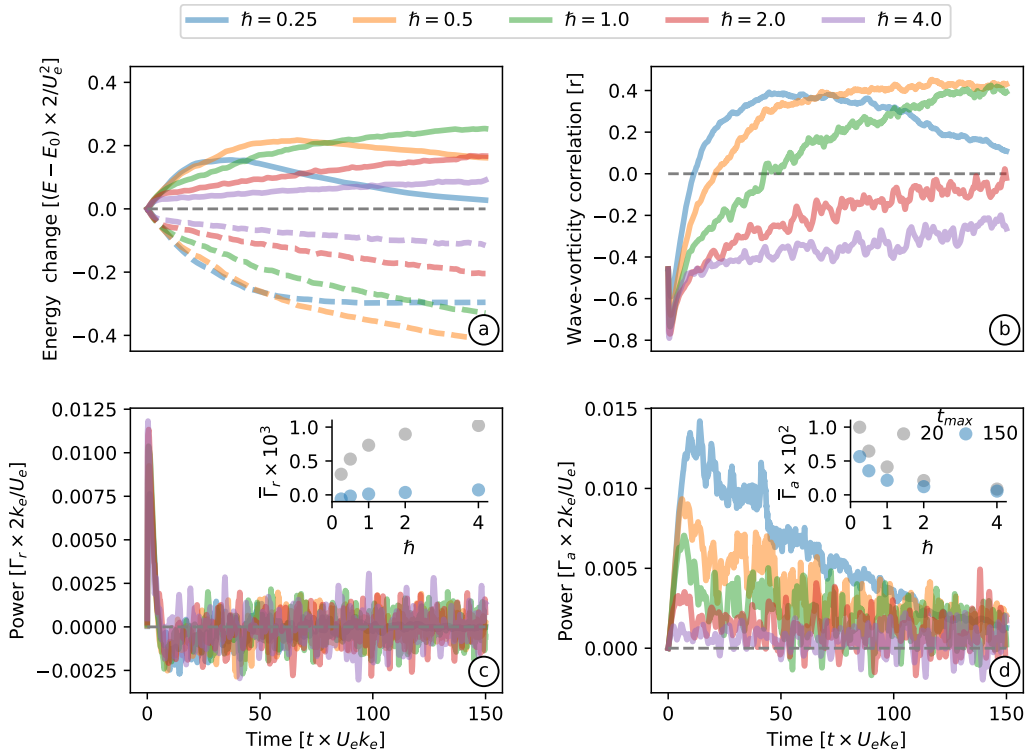


FIGURE 6. Statistics of the decaying turbulence solution with $\alpha \approx 1$ and different dispersivities, h . (a) Energy change about initial condition. (b) Coefficient of correlation between incoherent wave kinetic energy and relative vorticity (4.3). (c) Wave potential energy generation due to geostrophic refraction, Γ_r . (d) Wave potential energy generation due to geostrophic advection, Γ_a .

concentration in anticyclones, and the refraction conversion, Γ_r , decreases dramatically, reducing by half at $t \times U_e k_e \approx 3$. (Figure 5d). At this point, the Γ_a takes over the total energy conversion. At later time, $t \times U_e k_e > 5$, the refraction conversion is small in amplitude and oscillates about zero (Figure 5b). But the large Γ_a sustains the positive total energy conversion. The long-term wave field has scales smaller than the eddies and no wave concentration into anticyclones (Figure 5).

Wave potential energy accounts for about 18% of the bulk changes of geostrophic kinetic energy (Table 2). Advective conversion accounts for most of the energy change, representing about 98% of the bulk energy conversion. Direct dissipation accounts for about 6% of the loss of geostrophic kinetic energy. And the wave-dissipation source is significant: Ξ_r contributes about 7% of geostrophic kinetic energy gain.

Besides the energy extraction from the decaying turbulence flow, the waves also cause larger direct dissipation of geostrophic kinetic energy compared with a waveless QG solution with the same parameters (Appendix B). In the waveless solution the dissipation, ε_ψ , is about 2%, most of which occurs at $t \times U_e k_e < 20$. The direct dissipation of geostrophic kinetic energy is a consequence of the small-scale diffusion introduced in the potential vorticity equation (2.6). Hence, the stronger dissipation in the coupled model is due to finer scalar developed in the relative and potential vorticities, $\Delta\psi$ and q . Indeed, $\Delta\psi$ has more texture than waveless vorticity (compare figure 5 with figure C1), particularly outside the core of the vortices (Figure (5)b). The wave terms of the

potential vorticity are dominated by small scales and smaller than $\Delta\psi$ (Figure (5)c-d). Interestingly, much of the roughness in $\Delta\psi$ is canceled by the small-scale structures in the wave potential vorticity, yielding a smoother—but rougher than waveless QG—potential vorticity (compare figures 5 with figure C2).

5.3. Varying dispersivity

Figure 5 summarizes results from a set of solutions with varying the vertical wavelength $2\pi m^{-1}$ from 200 to 800 m, yielding dispersivities ranging from 0.25 to 4. (All other parameters are fixed.) The initial conversion due to refraction, $\Gamma_r(t \times U_e k_e < 20)$, increases slowly with \hbar (Figure 5c). The advective conversion, Γ_a , dominates the total conversion in all solutions. This term is largest for the weakest dispersivity regime and decays approximately exponentially with increasing dispersivity. Indeed, the initial wave potential energy growth sharpens with decreasing dispersivity. For the smallest dispersivity considered here, $\hbar = 0.25$, the wave potential energy peaks at $t \times U_e k_e \approx 25$, and then decays (see blue curve in figure 5a). This due to strong dissipation of wave potential energy because weak dispersion is ineffective in extenuating the generation of small scales by advection; the small scales created by geostrophic advection also implies strong direct dissipation of geostrophic kinetic energy. In other words, the quasi-inviscid weak-dispersion limit is inaccessible with fixed small-scale dissipation (fixed resolution) because geostrophic straining creates ever-finer scales of the wave field. (I'm running a simulation with double resolution to estimate how much energy transfer is curtailed by the strong dissipation in this simulation.)

The initial strong negative wave-vorticity correlation, caused by refraction, is equal in all case. But the reduction of this negative correlation, and eventual sign change, occurs faster with decreasing dispersivity. This is because, after the initial eddy-scale gradients are created, weakly dispersive waves extract much energy from the geostrophic flow via advective conversion, Γ_a (Figure 5d). The moderate to strong dispersion solutions, $\hbar > 1$ experience much slower decrease of correlation, and remains negative even after $t \times U_e k_e = 150$.

6. Discussion

The explicit expression for the energy conversion in (3.5) illuminates the physics of stimulated generation: both convergence of wave kinetic energy density in anticyclones and geostrophic straining are sources of wave potential energy and sinks of geostrophic kinetic energy. But this energy description of stimulated generation disguises the role of wave dispersion—waves can propagate out of the vorticity or straining regions, thereby reducing the correlations of the energy conversion in (3.5).

Indeed, wave dispersion is the only mechanism that upsets stimulated generation in the quasi-inviscid solutions described in sections 4 and 5. In all solutions, after an initial conversion due to refraction, geostrophic straining accounts for most of the energy conversion. But even in the weak dispersion solution, the waves not behave as a passive scalar. This is because geostrophic advection can only strain the near-inertial wave field so much. The near-inertial generalized group velocity is $f_0 \lambda^2 \nabla \Theta$ (cf. section 3), where Θ is the phase of the near-inertial back-rotated velocity: $\phi = |\phi| e^{i\Theta}$. With fixed dispersivity, $f_0 \lambda^2$, the very geostrophic straining, enhances the gradients $\nabla \Theta$, thereby increasing the near-inertial group velocity: the waves scape the straining region. Thus, the mechanism of wave capture (Bühler & McItyre 2005) does not occur in the solutions described above. Wave capture could occur if the flow lateral scale is much larger than the wave field. An extreme example is the elongation flow, $\psi = -\alpha xy$, in which the rate of strain is uniform.

While the geostrophic straining accounts for bulk energy transfers in the examples consider in 4 and 5, which represent a sink of 5 – 50% of the initial geostrophic kinetic energy, refraction plays a fundamental role in these solutions with uniform (laterally coherent) initial wave velocity. This initial condition idealized the generation of upper-ocean inertial oscillations by storms (e.g., Alford *et al.* 2016). And the rapid after storm loss of lateral coherence is a form of inertial pumping (Young & Ben Jelloul 1997; Klein *et al.* 2004), which is accompanied by an extraction of energy from the balanced flow by the waves. Once refraction reduced the lateral coherence of the waves, geostrophic advection begins to strain the wave field, thus starting the second stage of the energy extraction.

A secondary result of the analysis of the solutions in 4 and 5 is the strong time-dependence of the correlation between incoherent waves and the relative vorticity, which is a measure of the concentration of waves in cyclones or anticyclones (Danioux *et al.* 2015). Refraction attracts waves to anticyclones and expel them from cyclones, thereby generating a strong negative correlation. The subsequent decay of the negative correlation is partially accounted for by the unsteady advection, as conjectured by Danioux *et al.* (2015). Unsteady advection is compounded by the QG-NIW coupling: most of the initial energy extraction takes place in negative vorticity regions, which in turn weakens the anticyclones. For moderate to small dispersivity, the energy extraction is strong and the relative vorticity develops a positive skewness, thereby creating a positive wave-vorticity correlation.

There are numerous caveats to the application of our results to the complex after-storm oceanographic problem. Notably, the lack of geostrophic vertical shear suppresses important mechanisms of vertical refraction and straining, which introduce interesting modifications of the near-inertial wave physics (e.g., Thomas 2017) and can account for copious amounts of energy extraction by near-inertial waves (Shakespeare & Hogg 2017). Also, the focus on quasi-inviscid initial value problems undermines the role of dissipation—in forced-dissipative solutions, wave dissipation is likely to control the strength of stimulated generation. We plan to study the energy transfer associated with vertical shear and the role of forcing and dissipation in future studies.

This study was supported by the National Aeronautics and Space Administration and the National Science Foundation via grants NNX16AO5OH and OCE1357047.

Appendix A. Details of the QG-NIW model

A.1. The Xie & Vanneste (2015) model

Xie & Vanneste (2015) derive the QG-NIW model using a variational formulation of the generalized Lagrangian mean (GLM) framework with Whitham averaging. Following Young & Ben Jelloul (1997), Xie & Vanneste write the NIW velocity in complex form

$$u_w + iv_w = M_z e^{-if_0 t}. \quad (\text{A } 1)$$

Their derivation recovers the wave equation that governs the evolution of the NIW complex amplitude $\chi = iM/f_0$,

$$\chi_{zzt} + \partial_z J(\psi, \chi_z) + \frac{i}{2} \left[\left(\frac{N^2}{f_0} + \psi_{zz} \right) \Delta \chi - 2 \nabla \psi_z \cdot \nabla \chi_z + \chi_{zz} (\Delta \psi + 2\beta y) \right] = 0, \quad (\text{A } 2)$$

with the QG streamfunction $\psi(x, y, z, t)$. The QG flow evolves through stirring of QGPV

$$q_t + J(\psi, q) = 0. \quad (\text{A } 3)$$

A fundamental difference to [Young & Ben Jelloul \(1997\)](#) is that the potential vorticity in the [Xie & Vanneste \(2015\)](#) model contains quadratic wave terms

$$q = \nabla\psi + \left(\frac{f_0^2}{N^2}\psi_z\right)_z + \beta y + \frac{1}{2f_0}J(\chi_z^*, \chi_z) + \frac{1}{4f_0}(2|\nabla\chi_z|^2 - \chi_{zz}^*\nabla\chi - \chi_{zz}\nabla\chi^*), \quad (\text{A } 4)$$

thus NIWs affect the QG flow. The model of [Xie & Vanneste \(2015\)](#), with the potential vorticity that includes wave terms, generalizes early ideas introduced by [Bühler & McIntyre \(1998\)](#) to a setup that avoids spatial scale separation between geostrophic flow and waves, but restricts attention to near-inertial frequencies. Using standard perturbation theory, [Wagner & Young \(2016\)](#) recovered and extended this coupled QG-NIW system.

The special family of solutions with barotropic, f-plane QG flow, uniform background stratification, and single vertical mode NIW, $M_z = e^{imz} \phi(x, y)$, yields the reduced set of equations (2.6)-(2.7) used in this paper.

Appendix B. Details of the initial value problems

B.1. Small-scale dissipation

To absorb the forward cascade of enstrophy, we add a biharmonic diffusivity to the potential vorticity equation (2.6)

$$D_q = -\kappa_e \Delta^2 q, \quad (\text{B } 1)$$

where $\Delta^2 = (\partial_x^2 + \partial_y^2)^2$. Similarly, to prevent the development of very small scales, which may violate the near-inertial approximation, we add a biharmonic viscosity in the wave equation (2.7)

$$D_\phi = -\nu_w \Delta^2 \phi. \quad (\text{B } 2)$$

The hyperviscous terms add small dissipation to the energy equations in Section 2. The wave kinetic energy dissipation added to (3.3) is

$$\varepsilon_\phi \stackrel{\text{def}}{=} -\nu_w \langle |\Delta\phi|^2 \rangle. \quad (\text{B } 3) \quad \{\text{ep_phi}\}$$

The kinetic energy dissipation (B3) is associated only with the incoherent wave field, ϕ' , since $\Delta\langle\phi\rangle = 0$. Hyperviscosity also dissipates wave potential energy: the dissipation added to (3.5) is

$$\chi_\phi \stackrel{\text{def}}{=} -\nu_w \frac{\lambda^2}{2} \langle |\nabla\Delta\phi|^2 \rangle. \quad (\text{B } 4) \quad \{\text{chi_phi}\}$$

Similarly, the geostrophic kinetic energy dissipation added to (3.6) is

$$\varepsilon_q \stackrel{\text{def}}{=} \kappa_e \langle \psi \Delta q \rangle = \kappa_e \langle q \Delta^2 \psi \rangle, \quad (\text{B } 5) \quad \{\text{ep_q}\}$$

and the dissipation added to the potential enstrophy equation is

$$\chi_q \stackrel{\text{def}}{=} -\kappa_e \langle (\Delta q)^2 \rangle. \quad (\text{B } 6) \quad \{\text{chi_q}\}$$

Wave dissipation also adds two extra terms to the geostrophic kinetic energy budget:

$$\Xi = \underbrace{\frac{\nu_w}{2f_0} \langle \Delta\psi \frac{1}{2} (\phi^* \Delta^2 \phi + \phi \Delta^2 \phi^*) \rangle}_{\Xi_r} + \underbrace{\frac{\nu_w}{f_0} \langle \frac{1}{2} \psi [J(\phi^*, \Delta^2 \phi) - J(\phi, \Delta^2 \phi^*)] \rangle}_{\Xi_a}. \quad (\text{B } 7) \quad \{\text{xi}\}$$

TABLE 3. Description of parameters of Lamb-Chaplygin simulation.

Parameter	Description	Value	Unit
N	Number of modes	512	–
L_d	Domain size	$2\pi \times 200$	km
$2\pi k_e^{-1}$	Dipole radius	$L/15 \approx 84$	km
U_e	Dipole strength	5×10^{-2}	m s^{-1}
U_w	NIW speed	5×10^{-1}	m s^{-1}
$(U_e k_e)^{-1}$	Eddy turnover timescale	≈ 3	days
N_0	Buoyancy frequency	5×10^{-3}	s^{-1}
f_0	Colioris frequency	10^{-4}	s^{-1}
$2\pi m^{-1}$	NIW vertical wavelength	325	m
κ_e	QGPV biharmonic diffusivity	5×10^7	$\text{m}^4 \text{s}^{-1}$
ν_w	NIW biharmonic viscosity	5×10^7	$\text{m}^4 \text{s}^{-1}$

TABLE 4. Description of parameters of numerical simulations.

Parameter	Description	Value
N	Number of modes	512
L_d	Domain size	$2\pi \times 200$ km
$2\pi k_e^{-1}$	Centroid wavelength	$2\pi \times 50$ km
U_e	RMS velocity	0.1 m s^{-1}
U_w	NIW speed	0.14 m s^{-1}
N_0	Buoyancy frequency	10^{-2} s^{-1}
f_0	Colioris frequency	10^{-4} s^{-1}
$2\pi m^{-1}$	NIW vertical wavelength	$200 - 800$ m
κ_e	QGPV biharmonic viscosity	$5 \times 10^7 \text{ m}^4 \text{s}^{-1}$
ν_w	NIW biharmonic viscosity	$1 \times 10^6 \text{ m}^4 \text{s}^{-1}$

The term Ξ_r is easy to interpret: dissipation of wave kinetic energy, $\phi^* \Delta^2 \phi + \phi \Delta^2 \phi^* < 0$, in anticyclones, $\Delta\psi < 0$, represents a gain of geostrophic kinetic energy; this term is positive in all solutions of this paper. The second term, Ξ_a , is obscure, but it is also positive in all solutions. Hence, wave dissipation yields a gain of geostrophic kinetic energy.

In all solutions of initial value problems reported in this paper, the dissipative terms (B3), (B4), (B5), and (B7) account for less than 10% of the energy tendencies. The energy budgets close within 10^{-5} %.

B.2. Numerical methods

We solve the QG-NIW system (2.6)-(2.7) using a standard collocation Fourier spectral method. In the pseudo-spectral spirit, we evaluate the quadratic non-linearities in physical space, and transform the product into Fourier space. We time march the spectral equations using an exponential time differencing method with a fourth order Runge-Kutta scheme (details in Kassam & Trefethen 2005).

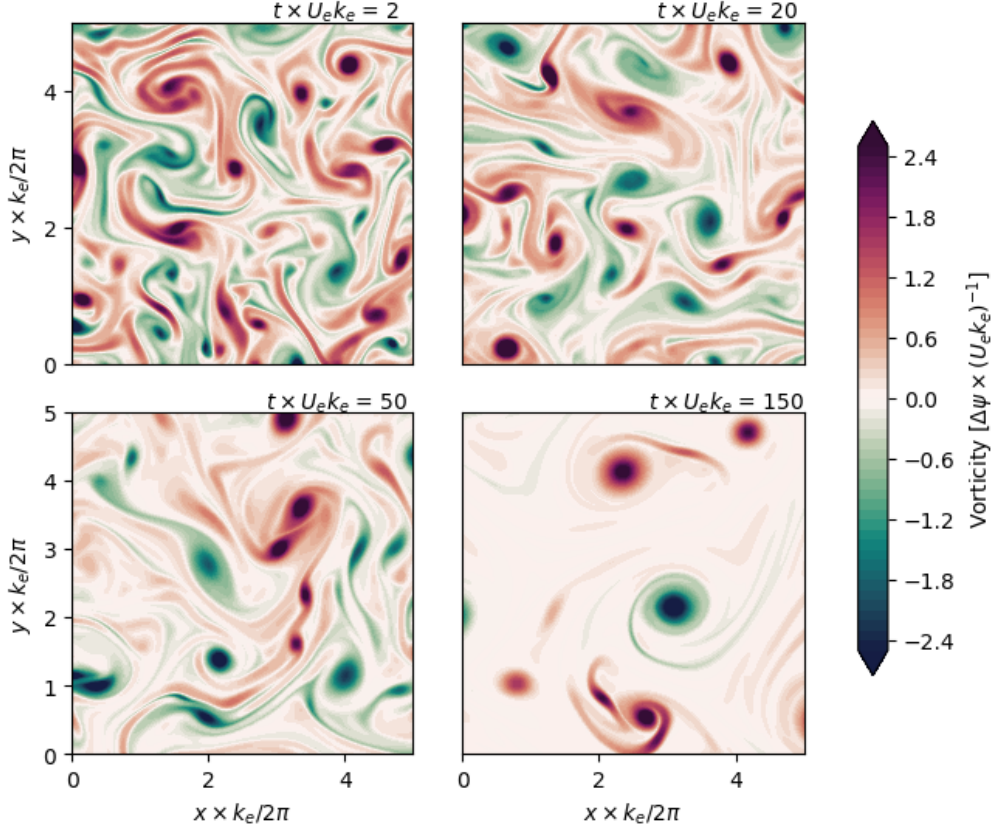


FIGURE 7. Snapshots of vorticity $\Delta\psi$ of a waveless macroturbulence reference solution (standard barotropic QG dynamics). The contours are the same as those of the figures in the main text.

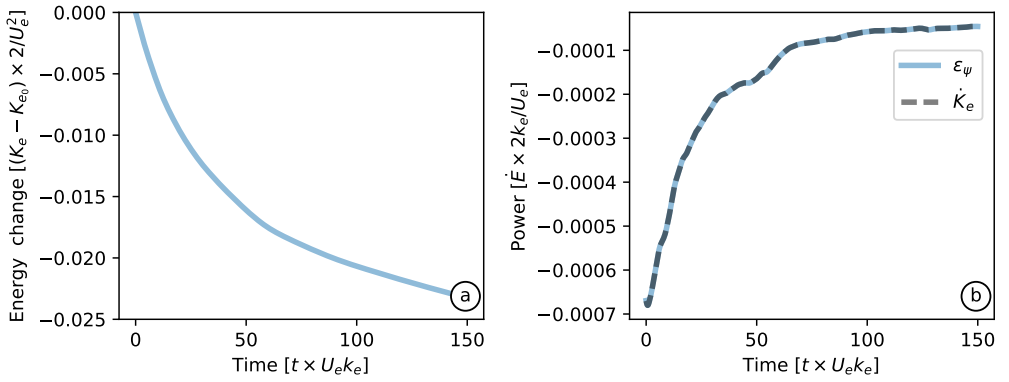


FIGURE 8. (a) The kinetic energy fractional change about initial condition and (b) the energy budget of the waveless macroturbulence reference solution.

B.3. Parameters

B.4. Reference waveless solution

B.5. Code and data

Our python code that solves (2.6)-(2.7) on a doubly periodic domain is available through a sustainable online repository (<https://github.com/crocha700/niwqg>). The code is well tested and documented. We used version 0.1 in this study.

The data used to plot figures 1-6 are available on the repository of the paper: https://github.com/crocha700/RochaWagnerYoung_JFM. To ensure reproduction and assist future studies, we also share the scripts that setup and run the simulations and analyze the results of this paper.

REFERENCES

- ALFORD, MATTHEW H, MACKINNON, JENNIFER A, SIMMONS, HARPER L & NASH, JONATHAN D 2016 Near-inertial internal gravity waves in the ocean. *Annual review of marine science* **8**, 95–123.
- BARKAN, ROY, WINTERS, KRAIG B & MCWILLIAMS, JAMES C 2016 Stimulated imbalance and the enhancement of eddy kinetic energy dissipation by internal waves. *Journal of Physical Oceanography* (2016).
- BÜHLER, OLIVER & MCINTYRE, MICHAEL E 1998 On non-dissipative wave–mean interactions in the atmosphere or oceans. *Journal of Fluid Mechanics* **354**, 301–343.
- BÜHLER, OLIVER & MCITYRE, M E 2005 Wave capture and wave–vortex duality. *Journal of Fluid Mechanics* **534**, 67–95.
- DANIOUX, ERIC, VANNESTE, JACQUES & BÜHLER, OLIVER 2015 On the concentration of near-inertial waves in anticyclones. *Journal of Fluid Mechanics* **773**, R2.
- D’ASARO, ERIC A, ERIKSEN, CHARLES C, LEVINE, MURRAY D, PAULSON, CLAYTON A, NILER, PETER & VAN MEURS, PIM 1995 Upper-ocean inertial currents forced by a strong storm. part i: Data and comparisons with linear theory. *Journal of physical oceanography* **25** (11), 2909–2936.
- FERRARI, RAFFAELE & WUNSCH, CARL 2009 Ocean circulation kinetic energy: Reservoirs, sources, and sinks. *Annual Review of Fluid Mechanics* **41** (1), 253.
- FORNBERG, BENGT 1977 A numerical study of 2-D turbulence. *Journal of Computational Physics* **25** (1), 1–31.
- KASSAM, ALY-KHAN & TREFETHEN, LLOYD N 2005 Fourth-order time-stepping for stiff pdes. *SIAM Journal on Scientific Computing* **26** (4), 1214–1233.
- KLEIN, PATRICE, LLEWELLYN SMITH, STEFAN & LAPEYRE, GUILLAUME 2004 Organization of near-inertial energy by an eddy field. *Quarterly Journal of the Royal Meteorological Society* **130** (598), 1153–1166.
- KUNZE, ERIC 1985 Near-inertial wave propagation in geostrophic shear. *Journal of Physical Oceanography* **15** (5), 544–565.
- LANDAU, LEV DAVIDOVICH & LIFSHITZ, EVGENII MIKHAILOVICH 2013 *Quantum mechanics: non-relativistic theory*, , vol. 3. Elsevier.
- MCWILLIAMS, JAMES C 1984 The emergence of isolated coherent vortices in turbulent flow. *Journal of Fluid Mechanics* **146**, 21–43.
- MELESHKO, VV & VAN HEIJST, GJF 1994 On Chaplygin’s investigations of two-dimensional vortex structures in an inviscid fluid. *Journal of Fluid Mechanics* **272**, 157–182.
- NAGAI, TAKEYOSHI, TANDON, AMIT, KUNZE, ERIC & MAHADEVAN, AMALA 2015 Spontaneous generation of near-inertial waves by the Kuroshio Front. *Journal of Physical Oceanography* **45** (9), 2381–2406.
- SHAKESPEARE, CALLUM J & HOGG, ANDREW MCC 2017 Spontaneous surface generation and interior amplification of internal waves in a regional-scale ocean model. *Journal of Physical Oceanography* (2017).
- TAYLOR, STEPHANNE & STRAUB, DAVID 2016 Forced Near-Inertial Motion and Dissipation of Low-Frequency Kinetic Energy in a Wind-Driven Channel Flow. *Journal of Physical Oceanography* **46** (1), 79–93.

- WAGNER, GL & YOUNG, WR 2015 Available potential vorticity and wave-averaged quasi-geostrophic flow. *Journal of Fluid Mechanics* **785**, 401–424.
- WAGNER, GL & YOUNG, WR 2016 A three-component model for the coupled evolution of near-inertial waves, quasi-geostrophic flow and the near-inertial second harmonic. *Journal of Fluid Mechanics* **802**, 806–837.
- XIE, J-H & VANNESTE, JACQUES 2015 A generalised-lagrangian-mean model of the interactions between near-inertial waves and mean flow. *Journal of Fluid Mechanics* **774**, 143–169.
- YOUNG, WR & BEN JELLOUL, MAHDI 1997 Propagation of near-inertial oscillations through a geostrophic flow. *Journal of marine research* **55** (4), 735–766.